

SALT spectroscopy of the HMXB associated with the LMC supernova remnant MCSNR J0513–6724

V. V. Gvaramadze^{*},^{1,2,3} A. Y. Kniazev,^{4,5,1,6}† N. Castro⁷ and I. Y. Katkov^{8,9,1}

¹*Sternberg Astronomical Institute, Lomonosov Moscow State University, Universitetskij Pr. 13, Moscow 119992, Russia*

²*Space Research Institute, Russian Academy of Sciences, Profsoyuznaya 84/32, Moscow 117997, Russia*

³*E. Kharadze Georgian National Astrophysical Observatory, Abastumani 0301, Georgia*

⁴*South African Astronomical Observatory, PO Box 9, 7935 Observatory, Cape Town, South Africa*

⁵*Southern African Large Telescope Foundation, PO Box 9, 7935 Observatory, Cape Town, South Africa*

⁶*Special Astrophysical Observatory, Nizhnij Arkhyz, Karachai-Circassia, 369167, Russia*

⁷*Leibniz-Institut für Astrophysik, An der Sternwarte 16, 14482 Potsdam, Germany*

⁸*New York University Abu Dhabi, Saadiyat Island, PO Box 129188, Abu Dhabi, UAE*

⁹*Center for Astro, Particle, and Planetary Physics, NYU Abu Dhabi, PO Box 129188, Abu Dhabi, UAE*

Accepted . Received

ABSTRACT

We report the results of optical échelle spectroscopy with the Southern African Large Telescope (SALT) of the mass donor star BSDL 923 in the neutron star high-mass X-ray binary XMMU J051342.6–672412 associated with the LMC supernova remnant (SNR) MCSNR J0513–6724. We found that BSDL 923 is a B0.7 III star with double peaked emission lines originating in a circumbinary disk-like structure. This classification and the presence of double-peaked emission lines imply that BSDL 923 is a Be star. Modelling with the stellar atmosphere code FASTWIND was used to derive the effective temperature $T_{\text{eff}} = 27 \pm 1$ kK, surface gravity $\log g = 3.22 \pm 0.10$, projected rotational velocity $v \sin i \approx 100 \pm 45$ km s⁻¹, colour excess $E(B - V) = 0.53 \pm 0.05$ mag, and luminosity $\log(L_*/L_\odot) = 5.46 \pm 0.10$ of BSDL 923, as well as to show that the surface of this star is polluted with α -elements (O, Mg and Si) from the supernova ejecta. We found also that the NS is orbiting BSDL 923 in an eccentric ($e = 0.158 \pm 0.061$) orbit with the orbital period of 1.280 ± 0.006 d and the semi-major axis of $17 \pm 3 R_\odot$, and the radius of BSDL 923 is $25 \pm 5 R_\odot$. We speculate that the NS is embedded in the atmosphere of BSDL 923 either because it was kicked at birth towards this star or because of inflation of BSDL 923 caused by the energy input from the supernova blast wave. Using long-slit spectroscopy with SALT, we searched for possible signs of the SNR shell in the 2D spectrum, but did not find them. This lack of detection is consistent with the young age ($\approx 4_{-1}^{+2}$ kyr) of MCSNR J0513–6724, implying that it is still in the adiabatic (non-radiative) phase.

Key words: stars: emission-line, Be – stars: individual: BSDL 923 – stars: massive – ISM: supernova remnants – X-rays: binaries.

1 INTRODUCTION

MCSNR J0513–6724 belongs to a rare group of supernova remnants (SNRs) associated with neutron star (NS) high-mass X-ray binaries (HMXBs). Currently, only six such associations are known. One in our Galaxy: SNR G322.1+00.0/Cir X-1 (Heinz et al. 2013;

Linares et al. 2010). Two in the Small Magellanic Cloud: MCSNR J0127–7332/SXP 1062 (Hénault-Brunet et al. 2012; Haberl et al. 2012; Gvaramadze et al. 2021) and MCSNR J0103–7201/SXP 1323 (Gvaramadze, Kniazev & Oskinova 2019a). And the other three in the Large Magellanic Cloud (LMC): MCSNR J0536–6735/CXOU J053600.0–673507 (Seward et al. 2012; Corbet et al. 2016; van Soelen et al. 2019), MCSNR J0513–6724/XMMU J051342.6–672412 (Maitra et al. 2019) and MCSNR J0507–6847/XMMU J050722.1–684758

* Deceased

† E-mail: a.kniazev@sao.nrf.co.za

(Maitra et al. 2021). The discovery of these associations is a big surprise, since it was believed that the characteristic formation time of HMXBs is several orders of magnitude longer than the lifetime of SNRs (e.g. Tauris & van den Heuvel 2006). The study of these objects is of great interest for various fields of astrophysics.

Spectroscopic observations of SNRs can be used to establish the type of supernova (SN) explosion that led to their formation (e.g. Seitenzahl et al. 2018) or to measure their expansion velocity and thereby to determine their age and at what stage of evolution they are (e.g. Lozinskaya 1992; Gvaramadze et al. 2019a, 2021). The latter in turn provides constraints on the models proposed to explain the origin of their associated HMXBs. In particular, knowledge of the age of HMXBs is necessary for constructing models of magnetic field and spin evolution of young NSs in binary systems (e.g. Shakura et al. 2012; Fu & Li 2012; Christodoulou, Laycock & Kazanas 2018; Ho et al. 2020; Wang & Tong 2020).

Spectroscopic observations of mass donor stars in HMXBs, in turn, are necessary to determine whether they are Be or supergiant HMXBs (e.g. van Kerkwijk, van Oijen & van den Heuvel 1989; McBride et al. 2008), to measure chemical abundances on their surfaces, and potentially to detect abundance anomalies caused by the pollution by SN ejecta (cf. Israelian et al. 1999; Gvaramadze et al. 2017). Spectroscopic observations are also needed to determine orbital parameters of HMXBs, such as their orbital periods, eccentricities, mass functions, and so on (e.g. van Kerkwijk et al. 1985; Townsend et al. 2011). The latter parameters can be used to infer SN kick velocities imparted to new-born NSs, to determine orbital parameters of pre-SN binaries and evolution of their post-SN orbits (e.g. Hills 1983; Tauris et al. 1999), and ultimately to find out final fates of HMXBs (e.g. Bhattacharya & van den Heuvel 1991; van den Heuvel 2019).

In this paper, we report the results of optical spectroscopic observations of the mass donor star BSDL 923 in the HMXB XMMU J051342.6–672412 associated with the LMC SNR MCSNR J0513–6724 with the Southern African Large Telescope (SALT). In Section 2, we review what is known about XMMU J051342.6–672412 and its host SNR. The SALT observations are described in Section 3 and analysed in Section 5. In Section 4, we analyse the TESS (Transiting Exoplanet Survey Satellite) data for XMMU J051342.6–672412. The obtained results are discussed in Section 6 and summarized in Section 7.

2 LMC SNR MCSNR J0513–6724 AND ITS ASSOCIATED HMXB XMMU J051342.6–672412

Maitra et al. (2019) detected an X-ray source of luminosity of $L_X \approx 7 \times 10^{33} \text{ erg s}^{-1}$ at the geometrical centre of the candidate SNR MCSNR J0513–6724 (Bozzetto et al. 2017) using data from *XMM-Newton*. An inspection of the X-ray light curve of this source revealed 4.4 s tentative pulsations, which were attributed to the NS spin period. Maitra et al. (2019) also identified an optical counterpart to the X-ray

Table 1. Properties of BSDL 923.

Spectral type	B0.7 III	This paper
RA(J2000)	05 ^h 13 ^m 42 ^s .60	2MASS
Dec.(J2000)	−67°24′10″.1	2MASS
<i>U</i> (mag)	12.97 ± 0.03	Zaritsky et al. (2004)
<i>B</i> (mag)	13.75 ± 0.03	Zaritsky et al. (2004)
<i>V</i> (mag)	13.45 ± 0.04	Zaritsky et al. (2004)
<i>I_c</i> (mag)	13.11 ± 0.04	Zaritsky et al. (2004)
<i>J</i> (mag)	12.93 ± 0.03	2MASS
<i>H</i> (mag)	12.84 ± 0.04	2MASS
<i>K_s</i> (mag)	12.69 ± 0.04	2MASS
3.6 μm (mag)	13.01 ± 0.03	IPAC 2009
4.5 μm (mag)	12.93 ± 0.03	IPAC 2009
5.8 μm (mag)	12.82 ± 0.07	IPAC 2009
8 μm (mag)	12.36 ± 0.14	IPAC 2009

source with the star BSDL 923¹ ($V \approx 13$ mag), whose spectral (B2.5) type and luminosity class (Ib) were obtained by Dachs (1972) from the $U - B$ and $B - V$ colours of the star and its membership of the LMC. The supergiant luminosity class of BSDL 923 was also derived by Maitra et al. (2019) on the basis of photometric measurements in a much wider spectral range. This suggests that the detected X-ray source is a supergiant HMXB. It was named XMMU J051342.6–672412 by Ho et al. (2020) and we will use this name hereafter.

The Optical Gravitational Lensing Experiment (OGLE) *I*-band light curve of BSDL 923 displays a nearly sinusoidal variability by about ± 0.15 mag over ≈ 19 yr and ≈ 0.05 mag variations within the half-yearly visibility windows (Maitra et al. 2019). After removing the long-term trend from the light curve and using the Lomb-Scargle (LS; Lomb 1976; Scargle 1982) technique, Maitra et al. (2019) found two strong peaks in the LS periodogram at 1.8025 and 2.2324 d. The latter (strongest) peak was interpreted as the likely orbital period of the HMXB.

In X-rays the SNR appears as an incomplete shell whose outer contour could be fitted by an ellipse with the semi-major and semi-minor axes of ≈ 60 and 50 arcsec respectively (see fig. 1 in Maitra et al. 2019). At the distance to the LMC of 49.9 kpc (Pietrzyński et al. 2013), the linear size of the SNR is $\approx 14 \text{ pc} \times 12 \text{ pc}$. From the X-ray spectral analysis of MCSNR J0513–6724, Maitra et al. (2019) determined the plasma temperature of $2.2_{-1.1}^{+1.2} \text{ keV}$. Assuming that the SNR is the Sedov phase and using the radius of the SNR of $\approx 14 \text{ pc}$, one can estimate the SNR expansion velocity and age of, respectively, $\approx 1400_{-400}^{+300} \text{ km s}^{-1}$ and $\approx 4000_{-1000}^{+2000} \text{ yr}$ (cf. Maitra et al. 2019). This makes XMMU J051342.6–672412 the youngest NS HMXB associated with a SNR known to date.

Maitra et al. (2019) also reported detection of MCSNR J0513–6724 in the Australian Square Kilometre Array Pathfinder (ASKAP) survey of the LMC at 888 MHz (Pennock et al. 2021). Their fig. 2 shows that the brightest radio emission spatially coincides with the region of the brightest and hardest X-ray emission, which supports the SNR interpretation of MCSNR J0513–6724. The further support

¹ Indicated in the SIMBAD data base as a post-AGB star candidate.

Table 2. Journal of the SALT observations.

Date	Grating	Exposure (sec)	Spectral scale (Å pixel ⁻¹)	Slit/Fiber (arcsec)	Seeing (arcsec)	Spectral range (Å)
Long-slit observations						
2019 October 10	PG2300	1400×2	0.26	1.50	2.2	6030–6870
Échelle observations						
2019 October 8	LR	2800×1	0.042	2.23	1.1	3840–8800
2019 October 11	LR	3000×1	0.042	2.23	1.2	3840–8800
2019 October 14	LR	3000×1	0.042	2.23	2.0	3840–8800
2020 October 06	MR	3000×1	0.042	2.23	1.1	3840–8800
2020 October 11	MR	3000×1	0.042	2.23	2.5	3840–8800
2020 October 18	MR	3000×1	0.042	2.23	1.5	3840–8800
2020 October 23	MR	3000×1	0.042	2.23	1.6	3840–8800
2020 October 31	MR	3000×1	0.042	2.23	2.0	3840–8800
2020 November 11	MR	3000×1	0.042	2.23	3.1	3840–8800
2020 November 27	MR	3000×1	0.042	2.23	2.8	3840–8800
2020 December 10	MR	3000×1	0.042	2.23	2.5	3840–8800

for this interpretation comes from the spectral index of the radio emission of $\alpha = -0.68 \pm 0.04$ (Maitra et al. 2019).

Table 1 summarizes some properties of BSDL 923. The coordinates and the JHK_s photometry are from the 2MASS All-Sky Catalog of Point Sources (Cutri et al. 2003). The $UBVI$ photometry is from the Magellanic Clouds Photometric Survey (Zaritsky et al. 2004). The 3.6, 4.5, 5.8 and 8 μm photometry is from the SAGE LMC and SMC IRAC Source Catalog (IPAC 2009) (Meixner et al. 2006).

3 SALT SPECTROSCOPY

To study BSDL 923 and to characterize the binary orbit, we obtained 11 spectra with the High-Resolution Spectrograph (HRS; Barnes et al. 2008; Bramall et al. 2010, 2012; Crause et al. 2014) on SALT (Buckley, Swart & Meiring 2006; O’Donoghue et al. 2006) in 2019–2020. Using this dual beam, fibre-fed échelle spectrograph, we obtained three spectra in the low resolution (LR) mode (the resolving power of $R = 14\,000 - 15\,000$) in 2019 and other 8 spectra in the medium resolution (MR) mode ($R = 36\,500 - 39\,000$; Kniazev et al. 2019) in 2020. In both modes the object and sky fibres have a 2.23 arcsec diameter. The resulting spectra in the blue and red arms cover the spectral range of $\approx 3700 - 8800$ Å. All but the first spectrum were obtained with an exposure of 3000 s, and the exposure of the first spectrum was 2800 s. The seeing during these observations was in the range from 1.1 to 3.1 arcsec. Spectra of a ThAr lamp and spectral flats were obtained for both modes during a weekly set of HRS calibrations.

Due to lower resolution and wider entrance slit, the LR HRS spectra have a better signal-to-noise (S/N) ratio ($S/N \sim 90$ at the maximum of an échelle order in the spectral region around the $H\beta$ line) than the MR HRS ones ($S/N \sim 60$ for the same spectral region). Correspondingly, the MR spectra were used only to measure the radial velocity of the star and to search for changes in profiles of strong spectral lines, while the LR spectra were also used for spectral classification and modelling.

Also, we carried out long-slit spectroscopic observations

of the field containing MCSNR J0513–6724 using the SALT Robert Stobie Spectrograph (RSS; Burgh et al. 2003; Kobulnicky et al. 2003). The observations were intended to search for possible signs of the SNR shell in the 2D spectrum and/or interaction of the SN blast wave with the local interstellar medium. The RSS spectra were taken on 2019 October 10 with a 1.5 arcsec slit (placed on BSDL 923 at position angle of $PA=20^\circ$) and the PG2300 grating, covering the spectral range of 6030–6870 Å. This setup provides a spectral resolution of FWHM of 2.20 ± 0.25 Å. Two 1400 s exposures were obtained under seeing conditions of 2.2 arcsec. For wavelength calibration of the spectra an Xe lamp arc spectrum was taken immediately after the science frames. A spectrophotometric standard star was observed with the same spectral setup for the relative flux calibration. An HRS spectrophotometric standard is observed once per month as a part of the HRS Calibration Plan. All HRS spectrophotometric standards have spectral distributions known in steps of 3–4 Å. We need to note here that SALT is a telescope with a variable pupil, so that the illuminating beam changes continuously during the observations. This makes absolute flux calibration impossible even when using spectrophotometric standards. However, the relative energy distributions are very accurate, especially as the SALT has an atmospheric dispersion compensator (ADC).

The obtained spectra were first reduced using the SALT science pipeline (Crawford et al. 2010). The further reduction of the échelle spectra was performed using the HRS pipeline described in Kniazev, Gvaramadze & Berdnikov (2016) and Kniazev et al. (2019). The long-slit spectra were further reduced as described in Kniazev (2022).

The journal of the SALT observations is given in Table 2.

4 TESS

TESS (Ricker et al. 2014) is a NASA Explorer-class mission aiming to image nearly the entire sky to search for exoplanets using the transit method. The standard TESS cadence is 30 min throughout a 30 d fixed-pointing “sector”.

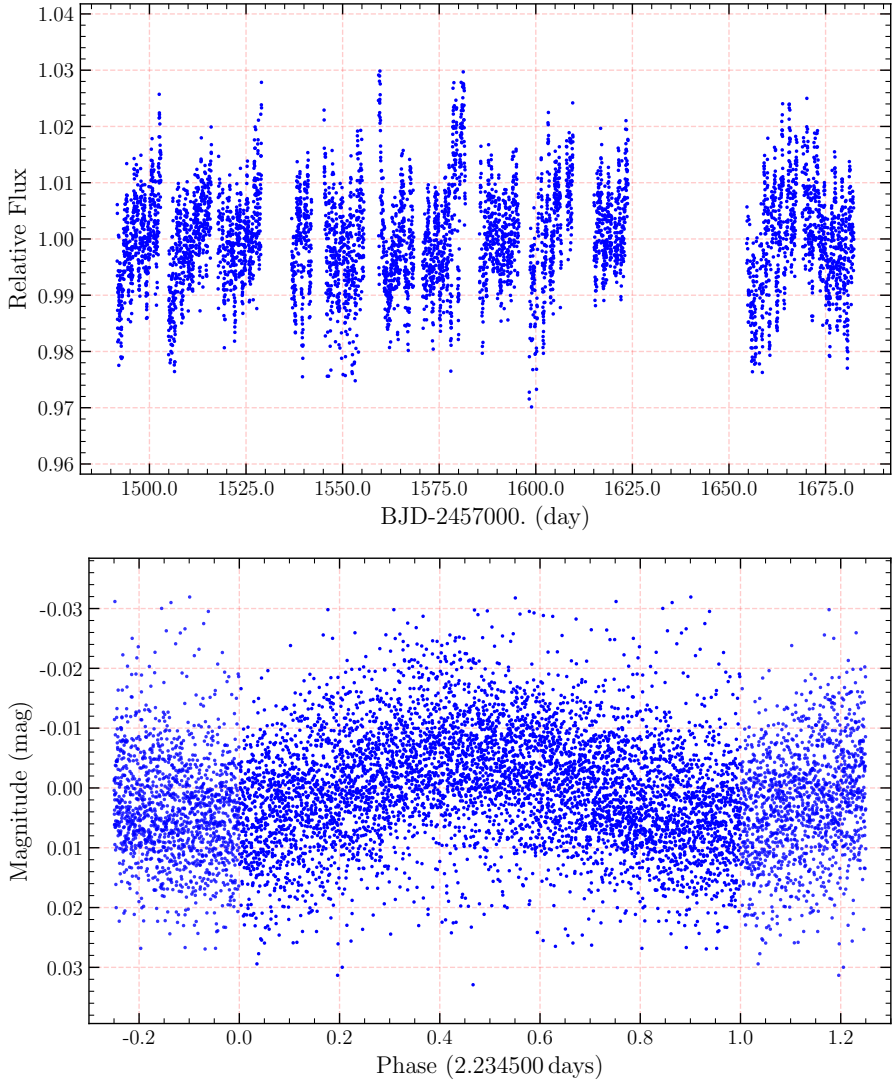


Figure 1. Top panel: The TESS light curve of BSDL 923 from the QLP pipeline (Huang et al. 2020ab). Bottom panel: The TESS light curve folded with a period of 2.2324 d.

The large part of reduced TESS data is publicly released and can be obtained from the Mikulski Archive for Space Telescopes (MAST)². In the current work, we use TESS light curves from the MIT quick-look pipeline (“QLP”; Huang et al. 2020ab)³. BSDL 923 was observed in the TESS sectors 7, 8, 9, 10, 11, and 13, which covered about half-year period with some holes in data related to data quality.

All available TESS data with quality flag 0 are shown in the top panel of Fig. 1. We analysed these photometric data in the same way as it was done in Maryeva et al. (2020). The Lomb-Scargle (LS) periodogram (Lomb 1976; Scargle 1982) using the MIDAS context TSA of these data (see Fig. 2) shows two significant peaks at periods of 2.2345 ± 0.0002 and 0.9165 ± 0.0001 d. The first of these periods is almost equal to the period of 2.2324 d obtained by Maitra et

al. (2019) from the analysis of the OGLE data (see Section 2), while their second period of 1.8025 d is just the second harmonic of the TESS peak at 0.9165 d; note that the one-day sampling period of the OGLE data did not allow Maitra et al. (2019) to detect periods shorter than 1 d. In Section 5.2, we show that none of the periods detected in the OGLE and TESS data are associated with the orbital period of XMMU J051342.6–672412. The bottom panel of Fig. 1 shows the TESS light curve folded with a period of 2.2324 d.

5 RESULTS OF SPECTROSCOPY

5.1 Spectral classification of BSDL 923

The spectrum of BSDL 923 (see Fig. 3) is dominated by the Balmer and He I lines, of which all He I and the higher-order Balmer lines are in absorption, while the $H\alpha$ and $H\beta$ lines are in emission. The latter line has a double-peaked profile

² <https://mast.stsci.edu>

³ See also <https://archive.stsci.edu/hlsp/qlp> for more details.

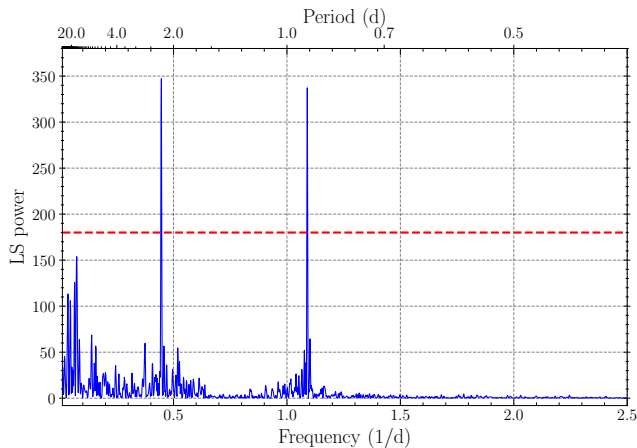


Figure 2. The LS periodogram of the TESS light curve of BSDL 923. The two strongest spikes correspond to periods of 2.2345 ± 0.0002 and 0.9165 ± 0.0001 d. The dashed (red) line shows the 5σ confidence level.

and is surrounded on both sides by photospheric absorption line wings. The spectrum also shows weak absorption lines of He II at 4200, 4542, 4686 and 5412 Å. Other double-peaked emission lines in the spectrum are due to Fe II. The near-infrared part of the spectrum shows lines of the Paschen series and persistent lines of neutral oxygen (O I $\lambda\lambda 7772$ –5, 8446), all of which are in emission and double-peaked as well. The double-peaked shape of the lines indicates that they originate in a flattened rotating structure, like an excretion disk around a Be star.

Comparison of the three LR HRS spectra revealed obvious changes in both emission and absorption line profiles. These changes are illustrated in Fig. 4 by the examples of three representative lines (H β , He I $\lambda 4922$ and Fe II $\lambda 6318$), which are shown in the reference frame of BSDL 923. We found that profiles of absorption lines in the first and third spectra do not differ much from each other, while in the second spectrum a red-shifted emission component has appeared in their cores.

To classify BSDL 923, we visually compared its spectrum with spectra of B stars in the LMC from Evans et al. (2015). For this, we merged the first and third LR HRS spectra after their correction for heliocentric motion, radial velocity variations (see Section 5.2) and redshift of the LMC, and then smoothed and degraded the resulting spectrum to the resolving power of $R = 4000$ used in Evans et al. (2015). We used only these two spectra because they are less affected by emission from the circumstellar material. Parts of the resulting spectrum, after normalization, are shown in Fig. 3.

The presence of He II lines indicates the spectral type earlier than B1 star, while the non-detection of the Si IV $\lambda 4116$ line and the nearly equal strength of the Si IV $\lambda 4089$ and Si III $\lambda 4553$ lines implies that BSDL 923 is either a B0.7 giant or a B0.5–B0.7 dwarf star (Evans et al. 2015; see also their figs A1–A3). The giant luminosity class is more preferable in view of the surface gravity derived for BSDL 923 in Section 5.3. We therefore conclude that BSDL 923 is a B0.7 III star. Although this classification and the presence of double-peaked emission lines imply that BSDL 923 is a

Be star and that XMMU J051342.6–672412 is a Be HMXB, the reality appears to be more interesting (see Section 6).

5.2 Radial velocity measurements and the orbital solution to XMMU J051342.6–672412

To characterize the binary orbit, we measured the heliocentric radial velocity, V_{hel} , of BSDL 923 using all 11 HRS spectra. For this, we utilized the FBS (Fitting Binary Stars) software developed by our group and described in Kniazev et al. (2020) and Kniazev (2020). The obtained values of V_{hel} are given in Table 3 along with dates of observations. To this table we also added EWs, FWHMs and heliocentric radial velocities of the H α line measured in each HRS spectrum.

Table 3 shows that V_{hel} is variable on a time scale of several days. To check whether this variability is described by one of the three possible orbital periods, 0.9165, 1.8025 or 2.2345 d, derived from the analysis of the OGLE and TESS data (see Sections 2 and 4), we fit the available data points to a binary model assuming that the binary components are point masses moving in Keplerian orbits. For that FBS software was used as well. The results of the fit are shown in Fig. 5 and summarized in Table 4.

From Table 4 it follows that none of the three periods fit the radial velocity measurements. It means that optical variations are not due to the system binarity, but have another reason, for example, due to the rotational modulation of B-star (e.g. Balona 2016) or due to the rotation of the circumbinary material (see Section 6 for more details).

Table 4 also shows that the systemic velocity of the binary system, γ , is equal to the systemic velocity of the local interstellar medium detected in the RSS spectrum (see Section 5.4) and agrees well with the local systemic velocity ($\approx 300 \text{ km s}^{-1}$) of the LMC (Kim et al. 1998), implying that the binary received a low or zero birth kick along our line of sight.

Moreover, Table 3 shows that despite the orbital motion of BSDL 923, the heliocentric radial velocity of the H α emission line (originating in the circumstellar medium) remains approximately equal to the systemic velocity of the binary system (we discuss this remarkable fact in the Section 6). In addition, we did not find any correlation between EW or FWHM of the H α line and the orbital phase, but found that EW tends to decrease with increasing FWHM (see Fig. 6).

5.3 Spectral modelling

Before proceeding with the stellar atmosphere modelling, we combined two of the three LR HRS spectra to increase S/N. The spectrum obtained on 2019 October 11 was discarded because it is strongly contaminated by emission from the circumstellar medium (see Section 5.1). The merged spectrum was rebinned reaching S/N of 140 in the spectral range used for modelling (see below).

The stellar atmosphere modelling was performed using the stellar atmosphere code FASTWIND (Santolaya-Rey, Puls & Herrero 1997; Puls et al. 2005). We followed the same technique and the stellar grid, for LMC metallicity, as described in Castro et al. (2012). Based on the effective temperature, T_{eff} , and gravity, $\log g$, derived by the algorithm, a tailored grid, exploring a large range of chemical abundances, was

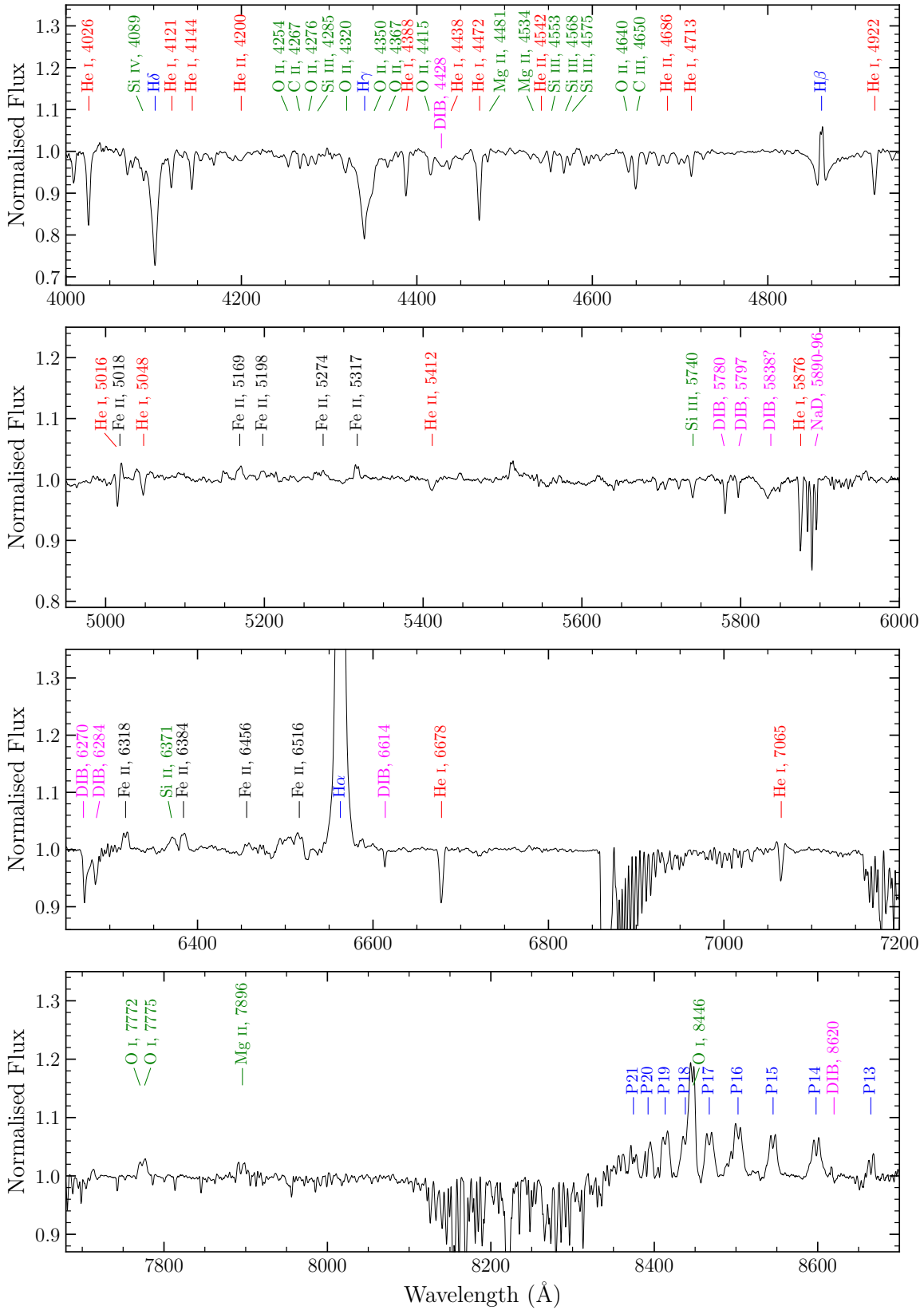


Figure 3. Portions of the normalized merged LR HRS spectra of BSDL 923 degraded to $R = 4000$ with main lines and diffuse interstellar bands (DIBs) indicated. The feature at 5520 Å is due to merging of échelle spectra obtained with the blue and red arms of HRS.

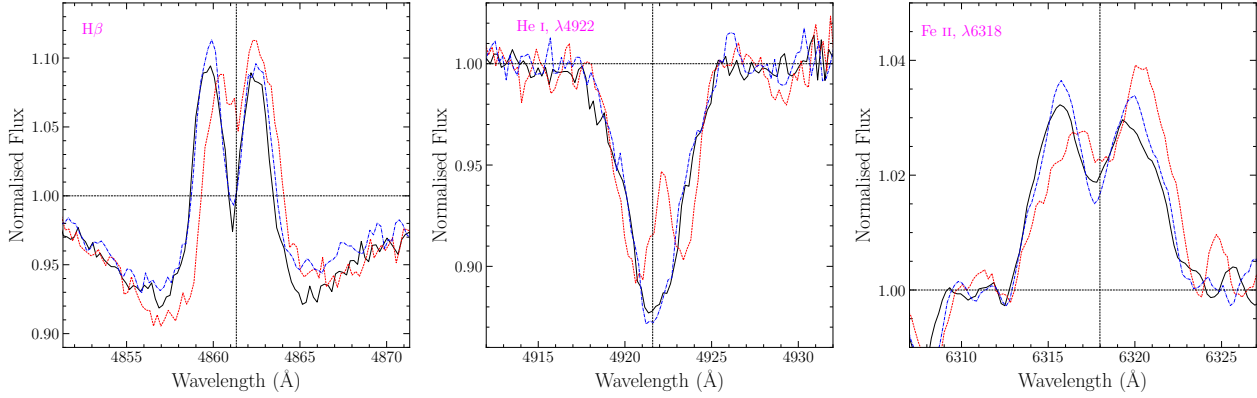


Figure 4. Profile variability of three representative lines in the LR HRS spectra of BSDL 923 obtained on 2019 October 8 (black solid line), 2019 October 11 (red dashed line) and 2019 October 14 (blue dot-dashed line). The lines are shown in the reference frame of BSDL 923.

Table 3. Heliocentric radial velocity, V_{hel} , of BSDL 923 and some parameters of the $H\alpha$ line measured at different orbital phases. ΔV is the difference between the observed values of V_{hel} and the model fit of the radial velocity curve of BSDL 923 to the Keplerian orbit.

Date	JD–2450000 (d)	V_{hel} (km s^{-1})	ΔV (km s^{-1})	Phase	EW($H\alpha$) (\AA)	FWHM($H\alpha$) (\AA)	$V_{\text{hel}}(H\alpha)$ (km s^{-1})
2019 October 8	8765.52109	313.8 ± 0.5	0.0022	0.76206	-17.5 ± 0.4	5.60 ± 0.02	312.47 ± 0.21
2019 October 11	8768.51130	287.8 ± 0.6	-2.4543	0.09877	-18.3 ± 0.4	5.53 ± 0.01	306.53 ± 0.11
2019 October 14	8771.52773	312.2 ± 0.4	0.2653	0.45597	-18.0 ± 0.5	5.10 ± 0.01	310.36 ± 0.12
2020 October 06	9129.55857	298.9 ± 0.6	0.8967	0.24050	-16.5 ± 0.3	5.65 ± 0.01	306.18 ± 0.17
2020 October 11	9134.52554	293.7 ± 0.6	2.8017	0.12196	-15.7 ± 0.2	6.02 ± 0.02	306.20 ± 0.26
2020 October 18	9141.56463	316.5 ± 0.5	-0.0628	0.62268	-16.2 ± 0.2	5.52 ± 0.01	309.26 ± 0.15
2020 October 23	9146.45694	311.3 ± 0.3	-0.1078	0.44580	-15.6 ± 0.2	5.47 ± 0.02	308.26 ± 0.24
2020 October 31	9154.49222	316.5 ± 0.7	1.1884	0.72499	-14.9 ± 0.2	6.86 ± 0.07	307.43 ± 0.90
2020 November 11	9165.43836	298.3 ± 0.8	-2.5654	0.27890	-16.2 ± 0.2	5.58 ± 0.02	306.97 ± 0.21
2020 November 27	9181.42116	311.5 ± 0.8	-1.9786	0.76872	-15.3 ± 0.2	6.16 ± 0.05	307.19 ± 0.52
2020 December 10	9194.40253	303.2 ± 1.2	1.9204	0.91306	-17.5 ± 0.2	5.47 ± 0.02	300.16 ± 0.23

built. The stellar parameters (including microturbulence ξ) and chemical abundances were derived through automatic algorithms searching for the set of parameters that best reproduce the main transitions in the range of ≈ 4000 – 5000 \AA (cf. Castro et al. 2012; Gvaramadze et al. 2014, 2019b).

The projected rotational and macroturbulence velocities, $v \sin i$ (where i is the inclination angle between the stellar rotational axis and the line-of-sight) and v_{mac} , were measured using the He I $\lambda 4387$ line and the IACOB-BROAD code (Simón-Díaz & Herrero 2007, 2014). We got $v \sin i = 100 \pm 45 \text{ km s}^{-1}$ and $v_{\text{mac}} = 150 \pm 50 \text{ km s}^{-1}$.

The colour excess, $E(B - V)$, and luminosity, L_* , of BSDL 923 were calculated using the photometry from Table 1 and the synthetic FASTWIND spectral energy distribution, and adopting a distance to the LMC of 49.9 kpc (Pietrzyński et al. 2013). We applied the extinction curves published by Fitzpatrick & Massa (2007) until the observed photometry was reproduced.

The best-fitting model for BSDL 923 is overlaid on the normalized observed spectrum in Fig. 7, while the stellar parameters and abundances derived in the model are given in Tables 5 and 6.

The colour excess and luminosity can also be derived in an independent way. To estimate $E(B - V)$ one can use the B and V photometry from Table 1 and the intrinsic

colour of a B0.7 III star of $(B - V)_0 = -0.25 \text{ mag}$ (extrapolated from Martins & Plez 2006), i.e. $E(B - V) = (B - V) - (B - V)_0 = 0.55 \pm 0.05 \text{ mag}$, which agrees well with the value given in Table 5. To derive the luminosity, we first estimate the absolute visual magnitude of BSDL 923: $M_V = V - DM - R_V E(B - V)$, where DM is the distance modulus of the LMC and R_V is the total-to-selective absorption ratio. Using $DM = 18.49 \text{ mag}$ (Pietrzyński et al. 2013) and $R_V = 3.1$, one finds $M_V = -6.74 \pm 0.16 \text{ mag}$. Taking a bolometric correction of $-2.63 \pm 0.08 \text{ mag}$ (Lanz & Hubeny 2007) the luminosity of BSDL 923 is $\log(L_*/L_\odot) = 5.64 \pm 0.10$, which agrees within the error margins with the value given in Table 5. Fig. 8 shows the position of BSDL 923 in the Hertzsprung-Russell diagram along with the show the MIST (MESA Isochrones and Stellar Tracks; Choi et al. 2016) evolutionary tracks of a 27–36 M_\odot single, LMC metallicity star. This result agrees with mass estimation $M_* = 37^{+31}_{-17} M_\odot$ presented in Section 6.

5.4 Spectroscopy of MCSNRJ0513–6724

We found no signs of the SNR shell in the 2D RSS spectrum. Fig. 9 plots the distribution of intensity profiles of the $H\alpha$, [N II] $\lambda 6584$ and combined [S II] $\lambda \lambda 6716, 6731$ lines (upper panel), and the $H\alpha$ heliocentric radial veloc-

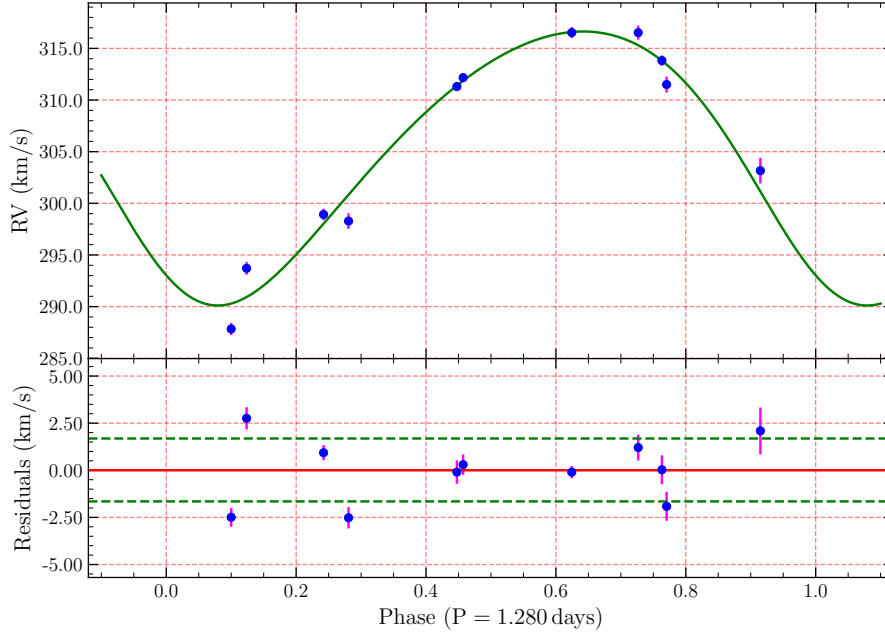


Figure 5. Upper panel: Radial velocity curve of BSDL 923 overlaid with a sine fit with a period of 1.280 ± 0.006 d to the heliocentric radial velocities listed in Table 3. Bottom panel: residuals of the fit, with a rms of 1.66 km s^{-1} .

Table 4. Orbital parameters of BSDL 923.

Parameter	Value
The closest epoch at periastron T_p (d)	2458764.5459 ± 0.1026
The superior conjunction phase ϕ_s	0.318
The inferior conjunction phase ϕ_i	0.893
Orbital period P (d)	1.280 ± 0.006
Eccentricity e	0.158 ± 0.061
Radial velocity semi-amplitude of the primary K (km s^{-1})	13.27 ± 0.84
Mass function $f(m) = (1 - e^2)^{3/2} PK^3 / 2\pi G$ (M_\odot)	$(2.98^{+0.71}_{-0.63}) \times 10^{-4}$
The longitude of the periastron ω (degrees)	141.72 ± 22.76
Systemic heliocentric velocity γ (km s^{-1})	305.02 ± 0.74
Root-mean-square residuals of Keplerian fit (km s^{-1})	1.66

Table 5. Parameters of BSDL 923.

Parameter	Value
T_{eff} (K)	$27\,000 \pm 1000$
$\log g$	3.22 ± 0.10
ξ (km s^{-1})	3 ± 1
v_{macro} (km s^{-1})	150 ± 50
$v \sin i$ (km s^{-1})	100 ± 45
$E(B - V)$ (mag)	0.53 ± 0.05
$\log(L_*/L_\odot)$	5.46 ± 0.10

Table 6. Metal abundances (by number) in BSDL 923. The present-day chemical composition of the LMC from Hunter et al. (2007) are given for reference.

$\log(X/H) + 12$	BSDL 923	LMC
C	7.69 ± 0.15	7.75
N	7.08 ± 0.20	6.90
O	8.76 ± 0.10	8.35
Mg	7.53 ± 0.20	7.05
Si	7.51 ± 0.15	7.20

ity profile (bottom panel) along the slit. In these plots MCSNRJ0513–6724 occupies the area between ≈ -50 and $+50$ arcsec. One can see that there is no brightness enhancements or a particularly strong [S II] emission at the edges of MCSNR J0513–6724, which is to be expected since this SNR is in the adiabatic (non-radiative) phase. Also, one can see that the heliocentric radial velocity of the $H\alpha$ emission towards the SNR does not differ much from the local systemic

velocity of the LMC of $\approx 300 \text{ km s}^{-1}$ (see fig. 3 in Kim et al. 1998), meaning that this emission originates in the background H II region not affected by the SN blast wave.

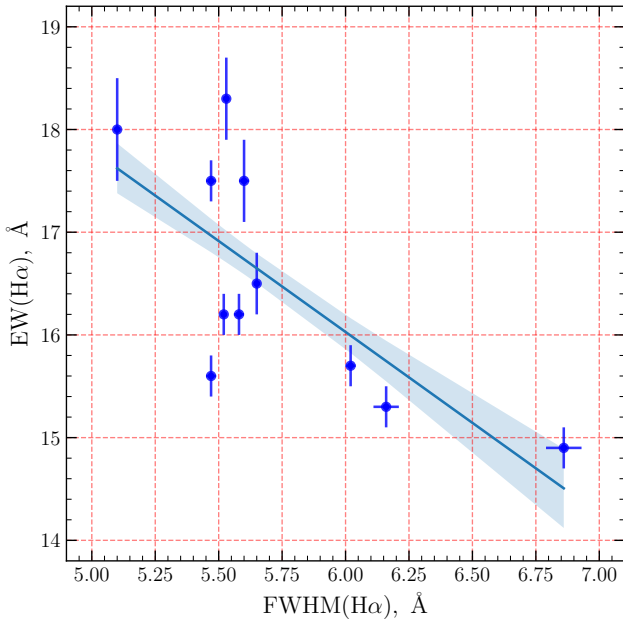


Figure 6. EW of the H α line as a function of its FWHM. The solid (blue) line is the least-squares linear fit. The shaded area is the 1σ uncertainty of the fit.

6 DISCUSSION

The results of spectral modelling could be used to derive the radius and mass of BSDL 923 through the following relations: $R_* = (L_*/4\pi\sigma T_{\text{eff}}^4)^{1/2}$ and $M_* = gR_*^2/G$, where σ and G are, respectively, the Stefan-Boltzmann and gravitational constants. Substituting the stellar parameters from Table 5 into these relations, gives $R_* = 25 \pm 5 R_\odot$ and $M_* = 37^{+31}_{-17} M_\odot$. With this mass one can calculate the semi-major axis of the NS orbit, a_{NS} , and estimate the orbital inclination angle i_{orb} . The former is given by

$$a_{\text{NS}} = \left[\frac{G(M_* + M_{\text{NS}})P^2}{4\pi^2} \right]^{1/3}, \quad (1)$$

where M_{NS} is the mass of the NS, while the latter could be determined from the following relation:

$$f(m) = \frac{M_{\text{NS}}^3 \sin^3 i_{\text{orb}}}{(M_* + M_{\text{NS}})^2}, \quad (2)$$

where the mass function $f(m)$ is given in Table 4. Adopting the canonical NS mass of $M_{\text{NS}} = 1.4 M_\odot$, one finds from equation (1) that $a_{\text{NS}} = 17 \pm 3 R_\odot$. Note that this estimate will remain almost the same if M_{NS} is allowed to change within the observed mass range for NSs of $\approx 1.2 - 2.0 M_\odot$ (e.g. Martinez et al. 2015; Cromartie et al. 2020).

To constrain the orbital inclination angle i_{orb} , we solved equation (2) using the mass ranges of $20 - 68 M_\odot$ and $1.2 - 2.0 M_\odot$ for BSDL 923 and the NS, respectively. Fig. 10 plots solutions to $f(m)$ for several values of i_{orb} . For $M_* = 37 M_\odot$ and $M_{\text{NS}} = 1.4 M_\odot$, one finds that $i_{\text{orb}} \approx 30^\circ$, but the uncertainty in the mass estimate for BSDL 923 implies that i_{orb} could range from $\approx 20^\circ$ to 55° (for $M_{\text{NS}} = 1.4 M_\odot$). Assuming that the stellar rotation axis is collinear with the

vector of the orbital momentum (i.e. $i = i_{\text{orb}}$)⁴, one finds that the surface rotational velocity of BSDL 923 could be as large as $\approx 300 \text{ km s}^{-1}$ (if $i_{\text{orb}} = 20^\circ$), which is not unheard of for OB stars of similar surface gravity (see fig. 1 in Brott et al. 2011).

The non-supergiant nature of BSDL 923 and the presence of double-peaked emission lines in its spectrum is typical of Be stars, implying that XMMU J051342.6–672412 might be a Be HMXB. If so, then the measured EW of the H α line of $\approx 20 - 25 \text{ \AA}$ (see Table 3) and the $P_{\text{orb}} - \text{EW}(\text{H}\alpha)$ diagram for Be HMXBs (see fig. 15 in Reig 2011) would imply that P_{orb} of XMMU J051342.6–672412 should be $\approx 60 - 80 \text{ d}$, i.e. a factor of $50 - 60$ longer than what follows from our analysis of the radial velocity curve of BSDL 923. On the other hand, the short spin and orbital periods of XMMU J051342.6–672412 place this HMXB in the leftmost bottom part of the Corbet diagram (Corbet 1986; see, e.g., fig. 2 in Reig 2011) populated by the very rare class of disk-fed supergiant HMXBs (currently, only three such objects are known). In these HMXBs the supergiant mass donor star overflows its Roche lobe and accretion on the NS occurs through an accretion disc, resulting in high (persistent) X-ray luminosity of $L_X \sim 10^{38} \text{ erg s}^{-1}$. The X-ray luminosity of XMMU J051342.6–672412 of $\sim 10^{34} \text{ erg s}^{-1}$ (Maitra et al. 2019), however, is about four orders of magnitudes lower and is more typical of wind-fed HMXBs, in which NSs accrete matter directly from the stellar wind. However, the Corbet diagram and $P_{\text{spin}} - P_{\text{orbit}}$ relation are relevant for systems near the spin equilibrium which is far from the case for such a young system as BSDL 923 (see below).

We note that the radial velocity measurements (see Section 5.2) show that the H α -emitting material does not participate in the orbital motion of BSDL 923. This indicates that this material does not form an accretion disk around BSDL 923 (i.e. this star is not a Be star), but is rather a rotating circumbinary disk-like structure. We plotted the H α -emitting material velocity versus photospheric velocities of BSDL 923 (both are presented in from Table 3) in Figure 11. The correlation coefficient between these two quantities is 0.47, which corresponds to a weak correlation.

We found that the radius of BSDL 923 is larger than the semi-major axis of the NS orbit, meaning that the NS is enveloped by BSDL 923. Moreover, since $M_{\text{NS}} \ll M_*$, the location of the second Lagrangian point L2 is approximately defined by the $R_{\text{L2}} \approx a_{\text{NS}} \left(1 + \sqrt[3]{M_{\text{NS}}/3M_*} \right) \approx 1.23 a_{\text{NS}}$, i.e. also inside BSDL 923. Such a situation, known as the common envelope phase (Paczynski 1976), usually occurs at advanced stages of evolution of the mass donor star in a binary system. But it could happen prematurely if the newly formed NS star received a kick of proper orientation and amplitude to become embedded in the secondary star (e.g. Leonard, Hills & Dewey 1994). Alternatively, the newborn NS could be engulfed in the secondary star due to inflation of its envelope caused by the energy input from the SN blast wave (e.g. Ogata, Hirai & Hijikawa 2021; cf. Johnston, Soria & Gibson 2016). The energy deposited in the star increases its radius and luminosity, and makes it

⁴ We caution that this may not be the case if the NS received a kick at birth.

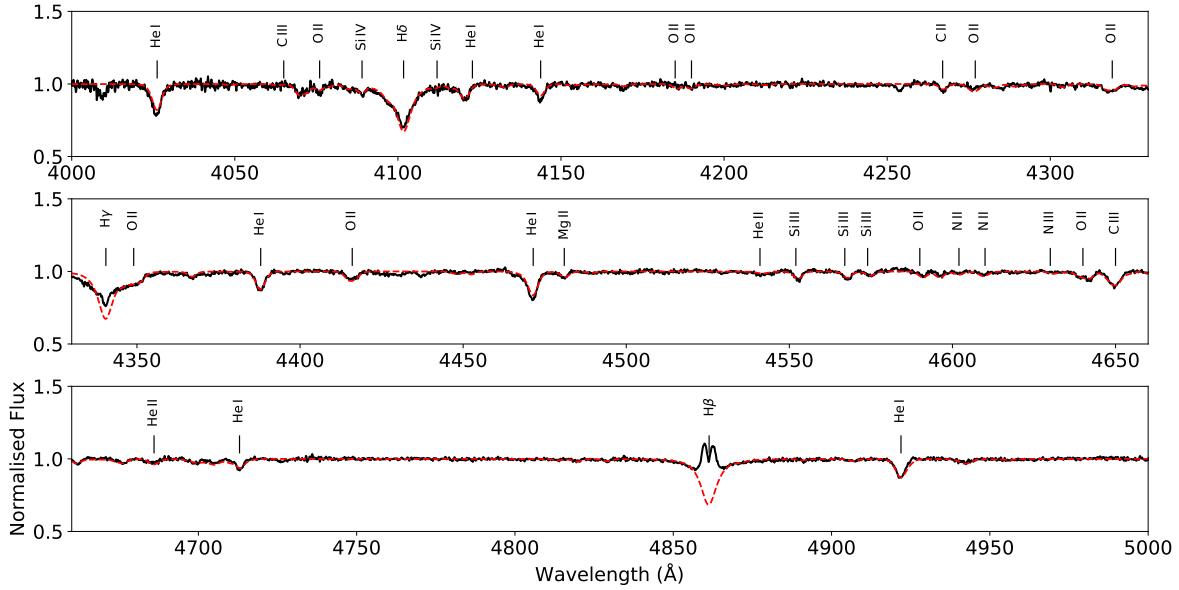


Figure 7. Normalized and re-binned spectrum of BSDL923 (black line) compared with the best-fitting FASTWIND model (red dashed line). The lines used to determine the stellar parameters (shown in Tables 5 and 6) are labeled.

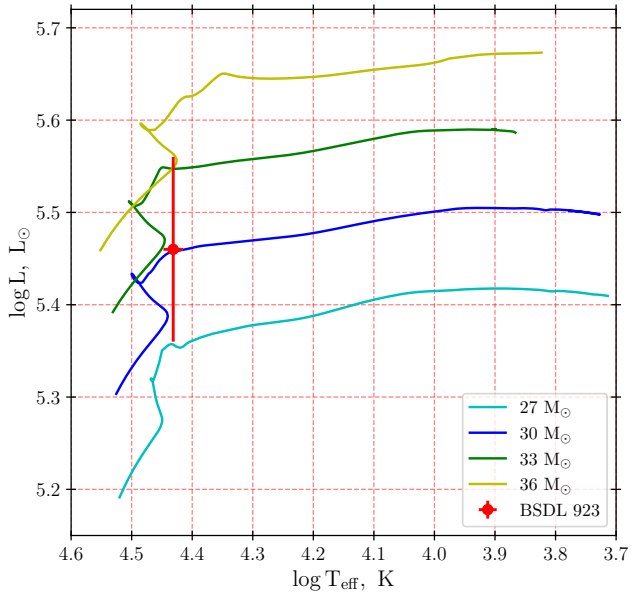


Figure 8. Position of BSDL923 (red symbol) in the Hertzsprung–Russell diagram. The solid lines of different colours show the MIST (Choi et al. 2016) evolutionary tracks of a 27–36 M_{\odot} single, LMC metallicity star.

underdense and cooler than a pristine star of the same initial mass and evolutionary phase. The time-scale for thermal adjustment (the Kelvin–Helmholtz time-scale) of such a perturbed star, $\tau_{\text{KH}} \approx (GM_*^2/2R_*L_*) \approx 3000$ yr, is comparable to the age of the SNR, meaning that BSDL923 could still remain bloated. In both cases, such a system will ultimately evolve in a Thorne–Żytkow object (Thorne & Żytkow 1975; Leonard et al. 1994; Hutlukejiang et al. 2018).

Which of the above two situations took place in

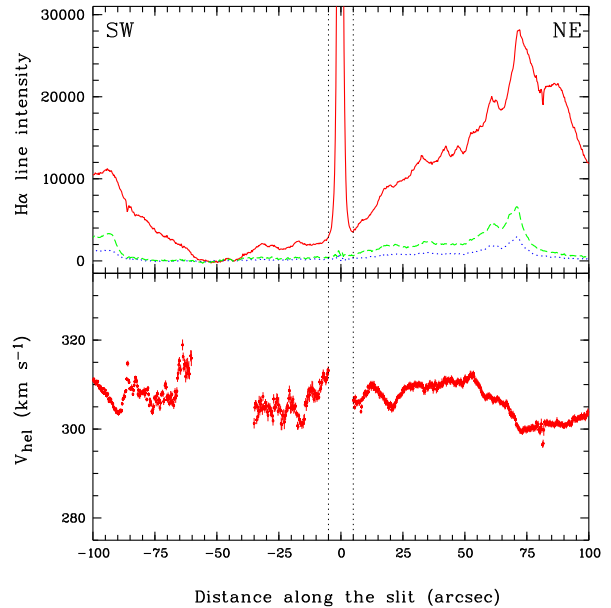


Figure 9. Upper panel: $\text{H}\alpha$, $[\text{N II}] \lambda 6584$ and combined $[\text{S II}] \lambda \lambda 6716, 6731$ line intensity profiles along the slit plotted by the (red) solid, (green) dashed and (blue) dotted lines, respectively. Bottom panel: $\text{H}\alpha$ heliocentric radial velocity profile along the slit. In both plots MCSNRJ0513–6724 occupies the area between ≈ -50 and $+50$ arcsec. Two vertical dashed lines (at ± 5 arcsec) mark the area where the radial velocity was not measured because of the effect of BSDL923. SW–NE direction of the slit is shown.

XMMU J051342.6–672412 is difficult to say, but in any case, it can be expected that the matter lost by BSDL923 should concentrate near the orbital plane forming a rotating disk-like structure responsible for the origin of two-peaked emission lines in the spectrum of this star. Since the common

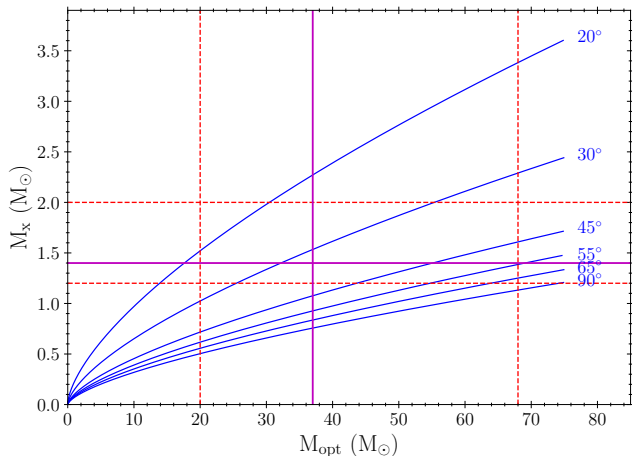


Figure 10. Mass-mass diagram of XMMU J051342.6–672412. The (blue) curves show the solution to the mass function for several values of the orbital inclination angle i_{orb} . The vertical solid line shows the mass of BSDL 923 of $37 M_{\odot}$ (with 1σ uncertainties shown by dashed lines). The horizontal solid line corresponds to a canonical NS mass of $1.4 M_{\odot}$, while the horizontal dashed lines indicate the observed range of NS masses of $1.2 - 2.0 M_{\odot}$.

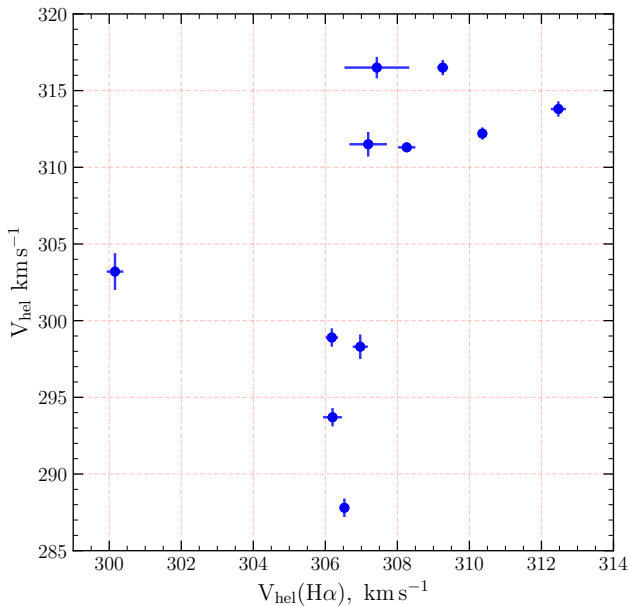


Figure 11. The H α -emitting material velocity versus photospheric velocity (radial velocity of BSDL 923).

envelope is not rotating as a rigid body (Paczynski 1976), one can expect that at least part of the material beyond L2 remains gravitationally bound to the system and that the rotational period of this circumbinary material is longer than the binary orbital period. It is therefore tempting to assume that the period of ≈ 2.23 d detected in both the OGLE and TESS light curves of BSDL 923 is associated with the rotational period of the circumbinary material.

Unlike the excretion disks in Be HMXBs (whose size is defined by the feedback from the companion NS), the size of

the circumbinary disk-like structure does not depend on the orbital period of the binary system, but could be limited by the high thermal pressure of gas in the interior of the SNR (cf. Gvaramadze et al. 2021).

Note that the short orbital period of the HMXB and the young age of the SNR (only several thousand years; see Section 2) imply that BSDL 923 may have peculiar chemical abundances due to pollution by SN ejecta. Interestingly, our spectral analysis did reveal enhanced abundances of several α -elements in the atmosphere of this star. Indeed, inspection of Table 6 shows that the measured abundances of carbon and nitrogen in BSDL 923 are in good agreement with the present-day abundances of these elements in the LMC, while abundances of the α -elements O, Mg and Si are $\approx 2.6 \pm 0.6$, $3.0^{+1.8}_{-1.1}$ and $2.0^{+0.9}_{-0.5}$ times enhanced. We interpret this as an indication that the surface of the star is contaminated by heavy elements from SN ejecta.

In conclusion, we note that a non-zero value of the orbital inclination angle means that the NS must be periodically eclipsed by BSDL 923. Correspondingly, the X-ray pulsations from the NS should be observable only at certain orbital phases before and after the superior conjunction (the duration of the eclipse phase depends on the orbital inclination angle and the density profile of the atmosphere of BSDL 923). Unfortunately, the relatively large uncertainty in P and the long time that has passed since the X-ray observations (lasting about a third of the orbital period) did not allow us to estimate the range of orbital phases covered by *XMM-Newton*.

7 SUMMARY

We have presented the results of high-resolution spectroscopic observations of the mass donor star BSDL 923 in the NS HMXB XMMU J051342.6–672412 associated with the LMC SNR MCSNR J0513–6724 carried out with the Southern African Large Telescope (SALT). We obtained 11 optical échelle spectra of BSDL 923, showing a distinct radial velocity variability, which reflects motion of the star in an eccentric ($e = 0.158 \pm 0.061$) orbit with a period of 1.280 ± 0.006 d. Our observations also showed that BSDL 923 is a B0.7 III star with a double peaked emission spectrum, and that despite the orbital motion of BSDL 923 the heliocentric radial velocity of the H α emission line (originating in the circumstellar medium) remains approximately equal to the systemic velocity of the binary system. This indicates that the double peaked emission lines originate in a rotating circumbinary disk-like structure.

Using the stellar atmosphere code FASTWIND, we derived some parameters of BSDL 923, such as its effective temperature, $T_{\text{eff}} = 27\,000 \pm 100$ K, surface gravity, $\log g = 3.22 \pm 0.10$, projected rotational velocity, $v \sin i \approx 100 \pm 45$ km s $^{-1}$, colour excess, $E(B - V) = 0.53 \pm 0.05$ mag, and luminosity $\log(L_* L_{\odot}) = 5.46 \pm 0.10$. Using these figures, we estimated the radius and mass of BSDL 923 to be, respectively, equal to $R_* = 25 \pm 5 R_{\odot}$ and $M_* = 37^{+31}_{-17} M_{\odot}$, which for the NS mass of $1.4 M_{\odot}$ gives the semi-major axis of the NS orbit of $a_{\text{NS}} = 17 \pm 3 R_{\odot}$, indicating that the NS is embedded in the atmosphere of BSDL 923. We have speculated that the NS find itself within the atmosphere of BSDL 923 either because it was kicked at birth towards the compan-

ion star or it became engulfed by the secondary star due to its inflation caused by the energy input from the SN blast wave. Another consequence of the encounter between the SN blast wave and BSDL 923 is that the stellar surface should be polluted by SN ejecta. Indeed, our spectral modelling has shown that abundances of the α -elements O, Mg and Si are enhanced by a factor of 2–3 compared to the present-day chemical composition of the LMC.

Also, we have carried out long-slit spectroscopy with SALT of the field containing MCSNR J0513–6724 in order to search for possible optical counterpart to the X-ray shell of the SNR and/or signs of interaction between the SN blast wave and the local interstellar medium. We did not find any brightness enhancement or a particularly strong [S II] emission in place of the X-ray shell which conforms with the young age (several thousand years) of MCSNR J0513–6724, implying that this SNR is in the adiabatic (non-radiative) phase.

8 ACKNOWLEDGEMENTS

This work is based on observations obtained with the Southern African Large Telescope (SALT), programmes 2019-1-MLT-002 and 2019-1-SCI-009, 2020-1-MLT-003, was supported by the National Research Foundation (NRF) of South Africa. AYK and IYK acknowledge the Ministry of Science and Higher Education of the Russian Federation grant 075-15-2022-262 (13.MNPMU.21.0003). NC acknowledges funding from the Deutsche Forschungsgemeinschaft (DFG) - CA 2551/1-1. This research has made use of the SIMBAD data base and the Vizier catalogue access tool, both operated at CDS, Strasbourg, France.

This paper is dedicated to the memory of Vasili Gvaramadze.

9 DATA AVAILABILITY

The data underlying this article will be shared on reasonable request to the corresponding author.

REFERENCES

- Balona L. A., 2016, *MNRAS*, 457, 3724
 Barnes S. I. et al., 2008, in McLean I. S., Casali M. M., eds, *Proc. SPIE Conf. Ser. Vol. 7014, Ground-based and Airborne Instrumentation for Astronomy II*. SPIE, Bellingham, p. 70140K
 Bhattacharya D., van den Heuvel E. P. J., 1991, *Phys. Rep.*, 203, 1
 Bozzetto L. M. et al., 2017, *ApJS*, 230, 2
 Bramall D. G. et al., 2010, in McLean I. S., Ramsay S. K., Takami H., eds, *Proc. SPIE Conf. Ser. Vol. 7735, Ground-based and Airborne Instrumentation for Astronomy III*. SPIE, Bellingham, p. 77354F
 Bramall D. G. et al., 2012, in McLean I. S., Ramsay S. K., Takami H., eds, *Proc. SPIE Conf. Ser. Vol. 8446, Ground-based and Airborne Instrumentation for Astronomy IV*. SPIE, Bellingham, p. 84460A
 Brott I. et al., 2011, *A&A*, 530, A115
 Buckley D. A. H., Swart G. P., Meiring J. G., 2006, in Stepp L. M., ed., *Proc. SPIE Conf. Ser. Vol. 6267, Ground-based and Airborne Telescopes*. SPIE, Bellingham, p. 62670Z
 Burgh E. B., Nordsieck K. H., Kobulnicky H. A., Williams T. B., O'Donoghue D., Smith M. P., Percival J. W., 2003, in Iye M., Moorwood A. F. M., eds, *Proc. SPIE Conf. Ser. Vol. 4841, Instrument Design and Performance for Optical/Infrared Ground-based Telescopes*. SPIE, Bellingham, p. 1463
 Castro N. et al., 2012, *A&A*, 542, A79
 Choi J. et al., 2016, *ApJ*, 823, 102
 Christodoulou D. M., Laycock S. G. T., Kazanas D., 2018, *MNRAS*, 478, 3506
 Corbet R. H. D., 1986, *MNRAS*, 220, 1047
 Corbet R. H. D. et al., 2016, *ApJ*, 829, 105
 Crause L. A. et al., 2014, in Ramsay S. K., McLean I. S., Takami H., eds, *Proc. SPIE Conf. Ser. Vol. 9147, Ground-based and Airborne Instrumentation for Astronomy V*. SPIE, Bellingham, p. 91476T
 Crawford S. M. et al., 2010, in Silva D. R., Peck A. B., Soifer B. T., *Proc. SPIE Conf. Ser. Vol. 7737, Observatory Operations: Strategies, Processes, and Systems III*. SPIE, Bellingham, p. 773725
 Cromartie H. T. et al., 2020, *Nature Astron.*, 4, 72
 Dachs J., 1972, *A&A*, 18, 271
 Evans C. J. et al., 2015, *A&A*, 574, A13
 Fitzpatrick E. L., Massa D., 2007, *ApJ*, 663, 320
 Fu L., Li X.-D., 2012, *ApJ*, 757, 171
 Gvaramadze V. V., Miroshnichenko A. S., Castro N., Langer N., Zharikov S. V., 2014, *MNRAS*, 437, 2761
 Gvaramadze V. V. et al., 2017, *Nature Astron.*, 1, 0116
 Gvaramadze V. V., Kniazev A. Y., Oskinova L. M., 2019a, *MNRAS*, 485, L6
 Gvaramadze V. V., Kniazev A. Y., Castro N., Grebel E. K., 2019b, *AJ*, 157, 53
 Gvaramadze V. V., Kniazev A. Y., Gallagher J. S., Oskinova L. M., Chu Y.-H., Gruendl R. A., Katkov I. Y., 2021, *MNRAS*, 503, 3856
 Haberl F., Sturm R., Filipović M. D., Pietsch W., Crawford E. J., 2012, *A&A*, 537, L1
 Heinz S. et al., 2013, *ApJ*, 779, 171
 Hénault-Brunet V. et al., 2012, *MNRAS*, 420, L13
 Hills J. G., 1983, *ApJ*, 267, 322
 Ho W. C. G., Wijngaarden M. J. P., Andersson N., Tauris T. M., Haberl F., 2020, *MNRAS*, 494, 44
 Howarth I. D., 1983, *MNRAS*, 203, 301
 Huang C.H. et al., 2020a, *Res. Notes Am. Astron. Soc.*, 4, 204
 Huang C.H. et al., 2020b, *Res. Notes Am. Astron. Soc.*, 4, 206
 Hunter I. et al., 2007, *A&A*, 466, 277
 Hutulukeyang B., Zhu C., Wang Z., Lü G., 2018, *JA&A*, 39, 21
 Israelian G., Rebolo R., Basri G., Casares J., Martin E. L., 1999, *Nature*, 401, 142
 Johnston H. M., Soria R., Gibson J., 2016, *MNRAS*, 456, 347
 Kim S., Staveley-Smith L., Dopita M. A., Freeman K. C., Sault R. J., Kesteven M. J., McConnell D., 1998, *ApJ*, 503, 674
 Kniazev A. Y., 2022, *AstBu*, 77, 334
 Kniazev A. Y., Gvaramadze V. V., Berdnikov L. N., 2016, *MNRAS*, 459, 3068
 Kniazev A. Y., Usenko I. A., Kovtyukh V. V., Berdnikov L. N., 2019, *Astrophys. Bull.*, 74, 208
 Kniazev A. Y., Malkov O. Y., Katkov I. Y., Berdnikov L. N., 2020, *Res. Astron. Astrophys.*, 20, 119
 Kniazev A. Y., 2020, *Ap&SS*, 365, 169
 Kobulnicky H. A., Nordsieck K. H., Burgh E. B., Smith M. P., Percival J. W., Williams T. B., O'Donoghue D., 2003, in Iye M., Moorwood A. F. M., eds, *Proc. SPIE Conf. Ser. Vol. 4841, Instrument Design and Performance for Optical/Infrared Ground-based Telescopes*. SPIE, Bellingham, p. 1634
 Lanz T., Hubeny I., 2007, *ApJS*, 169, 83
 Leonard P. J. T., Hills J. G., Dewey R. J., 1994, *ApJ*, 423, L19

- Linares M. et al., 2010, *ApJ*, 719, L84
- Lomb N. R., 1976, *Ap&SS*, 39, 447
- Lozinskaya T. A., 1992, *Supernovae and Stellar Wind in the Interstellar Medium*. Am. Inst. Phys., New York
- Maitra C. et al., 2019, *MNRAS*, 490, 5494
- Maitra C., Haberl F., Maggi P., Kavanagh P., Vasilopoulos G., Sasaki M., Filipovic M. D., Udalski A., 2021, *MNRAS*, 504, 326
- Martinez J.G. et al., 2015, *ApJ*, 812, 143
- Martins F., Plez B., 2006, *A&A*, 457, 637
- Maryeva O. V., Gvaramadze V. V., Kniazev A. Y., Berdnikov L. N., 2020, *MNRAS*, 498, 5093
- McBride V. A., Coe M. J., Negueruela I., Schurch M. P. E., McGowan K. E., 2008, *MNRAS*, 388, 1198
- Meixner M. et al., 2006, *AJ*, 132, 2268
- O'Donoghue D. et al., 2006, *MNRAS*, 372, 151
- Ogata M., Hirai R., Hijikawa K., 2021, *MNRAS*, 505, 2485
- Paczynski B., 1976, in Eggleton P., Mitton S., Whelan J., eds, *Proc. IAU Symp. 73, Structure and Evolution of Close Binary Systems*. Kluwer, Dordrecht, p. 75
- Pennock C.M. et al., 2021, *MNRAS*, 506, 3540
- Pietrzyński G. et al., 2013, *Nature*, 495, 76
- Puls J., Urbaneja M. A., Venero R., Repolust T., Springmann U., Jokuthy A., Mokiem M. R., 2005, *A&A*, 435, 669
- Reig P., 2011, *Ap&SS*, 332, 1
- Ricker G. R. et al., 2014, in Oschmann J. M. Jr, Clampin M., Fazio G. G., MacEwen H. A., eds, *Proc. SPIE Conf. Ser. Vol. 9143, Space Telescopes and Instrumentation 2014: Optical, Infrared, and Millimeter Wave*. SPIE, Bellingham, p. 15
- Santolaya-Rey A. E., Puls J., Herrero A., 1997, *A&A*, 323, 488
- Scargle J. D., 1982, *ApJ*, 263, 835
- Seitenzahl I. R., Vogt F. P. A., Terry J. P., Ghavamian P., Dopita M. A., Ruiter A. J., Sukhbold T., 2018, *ApJ*, 853, L32
- Seward F. D., Charles P. A., Foster D. L., Dickel J. R., Romero P. S., Edwards Z. I., Perry M., Williams R. M., 2012, *ApJ*, 759, 123
- Shakura N., Postnov K., Kochetkova A., Hjalmarsdotter L., 2012, *MNRAS*, 420, 216
- Simón-Díaz S., Herrero A., 2007, *A&A*, 468, 1063
- Simón-Díaz S., Herrero A., 2014, *A&A*, 562, A135
- Tauris T. M., van den Heuvel E. P. J., 2006, in Lewin W. H. G., van der Klis M., eds, *Formation and Evolution of Compact Stellar X-ray Sources*, Compact stellar X-ray sources. Cambridge Univ. Press, Cambridge, p. 623
- Tauris T. M., Fender R. P., van den Heuvel E. P. J., Johnston H. M., Wu K., 1999, *MNRAS*, 310, 1165
- Thorne K. S., Żytkow A. N., 1975, *ApJ*, 199, L19
- Townsend L. J., Coe M. J., Corbet R. H. D., Hill A. B., 2011, *MNRAS*, 416, 1556
- van den Heuvel, E. P. J. 2019, in Oskinova L., Bozzo E., Gies D., Holz D., eds, *Proc. IAU Symp. 346, High-mass X-ray Binaries: Illuminating the Passage from Massive Binaries to Merging Compact Objects*. Cambridge Univ. Press, Cambridge, p. 1
- van Kerkwijk M. H., van Oijen J. G. J., van den Heuvel E. P. J., 1989, *A&A*, 209, 173
- van Kerkwijk M. H., van Paradijs J., Zuiderwijk E. J., Hammerschlag-Hensberge G., Kaper L., Sterken C., 1995, *A&A*, 303, 483
- van Soelen B., Komin N., Kniazev A., Väisänen P., 2019, *MNRAS*, 484, 4347
- Wang W., Tong H., 2020, *MNRAS*, 492, 762
- Zaritsky D., Harris J., Thompson I. B., Grebel E. K., 2004, *AJ*, 128, 1606